

3D Printed Multilayer Graphite@SiO Structural Anode for High-Loading Lithium-Ion Battery

Wenjie He,^[a] Chenglong Chen,^[b] Jiangmin Jiang,^[a] Zhijie Chen,^[a] Haojie Liao,^[a] Hui Dou,^{*[a]} and Xiaogang Zhang^{*[a]}

To satisfy the increasing demand for higher energy density, the fabrication and structural designs of three-dimensional (3D) thick electrodes have received considerable attention. In this work, cheap commercial graphite (Gt) and silicon monoxide (SiO) were chosen as raw materials. We have took advantage of the multi-layer biscuit structure feature to the 3D Gt@GS (Gt@Gt/SiO) electrode with high loading through a modified 3D printing technology. Such a unique structure can not only effectively accommodate the volume expansion in all directions, but also provide a 3D transport channel to enhance the mobility of electrons and ions in the thick electrodes. The obtained 3D Gt@GS electrode, as a freestanding material, shows

high capacity and good cycling stability. Especially, the 3D Gt@GS electrode after 120 cycles has achieved a reversible capacity of 3.52 mAh cm^{-2} at 3.6 mA cm^{-2} .

In addition, we have successfully fabricated a 3D plane-shaped batteries *via* a direct ink writing technology and a fused deposition technology. The heterotypic battery assembled can be utilized as an external power supply for the aircraft model. This work demonstrates that the structural battery combined with structural load and 3D printing technology is versatile enough to meet the demand of energy storage systems for high energy density.

Introduction

As a result of the forthcoming demand for higher energy densities in electric vehicles and portable electronic devices, commercial lithium-ion batteries (LIBs) have received considerable attention. So far, most studies have focused on how to incorporate LIBs into a practical high-energy battery and what are needed to improve the high safety characteristics and cycle life.^[1–3] In general, for achieving higher energy density, LIBs can develop novel battery chemistries with a higher specific capacity, or increase the volume/mass ratio of active materials in the full battery design.^[2,4–7] In our daily lives, energy storage devices are increasingly used in various consumer electronics, electric aircraft and automobiles to power these devices. Provided that the battery itself can be used as a functional component of the device, it can provide electricity under mechanical loading.^[8–11] However, studies on structural energy storage are rarely reported now, especially in the direction of structural battery.

In today-LIBs, silicon-based materials have a high theoretical specific capacity and natural abundance relatively, which implies they can surpass the energy densities and workability of other anode materials.^[12–14] However, the huge stress derived from the volume variation leads to a poor cycling retention during operation. In order to improve electrochemical performance, much effort has been made to design unique nanostructures and composites with the flexible or rigid frameworks.^[12,15–17] Besides, the modified silicon-based materials also have a high probability of detaching from the current collector, because the volume expansion of the conventional thin film electrode is only buffered, but not completely gone. Therefore, when increasing the mass loading of the active material, electrodes are more prone to rupture and delamination, causing performance deterioration.^[18,19] Given silicon-based hybrid materials application, the attainment of high energy density in the future has an increasingly urgent demand for the design of thick electrodes.

The designs of thick electrodes in silicon-based materials not merely require favorable electron-transfer kinetics, but also need to reserve an effective space to preserve the electrolyte infiltrate and accommodate the volume expansion during cycles.^[20–22] In the last decade, the fabrication and structural designs of thick electrodes, such as laser processing,^[20–22] slurry-casting technique,^[24] layer-by-layer spray deposition,^[21] electrostatic-assisted self-assembly approach,^[25] suspension-casting method,^[26] roll-and-cut method,^[27] layer-by-layer assembly,^[28] aerosol jet printing^[29] and freeze-casting process^[30] were widely studied. Recently, the 3D printing technology has been constantly utilized in the thick electrode design.^[30] The thick array electrode by the 3D printing constructs the percolation network to supply a 3D electron transfer path. Simultaneously,

[a] Dr. W. He, Dr. J. Jiang, Dr. Z. Chen, H. Liao, Prof. H. Dou, Prof. X. Zhang
Jiangsu Key Laboratory of Electrochemical Energy Storage Technologies
College of Material Science and Technology
Nanjing University of Aeronautics and Astronautics
Nanjing, 210016, China
E-mail: dh_msc@nuaa.edu.cn
azhangxg@nuaa.edu.cn

[b] Dr. C. Chen
School of Chemical Engineering
Nanjing University of Science and Technology
Nanjing, 210094, China

 Supporting information for this article is available on the WWW under
<https://doi.org/10.1002/batt.202100258>

the electrolyte-filled space in the array electrode provides a fast ion transmission path. Additionally, the 3D printing can be used to fabricate the complex shaped electronics and energy devices, thus dramatically reducing material waste and costs, and providing conveniences for the design of the heterotypic battery.^[31–35] Unfortunately, there are no available guidelines on how to determine the appropriate 3D printing technique for silicon-based thick electrodes. The main reasons may be restrictions on the ink viscosity and the design of 3D architecture. Thus, it remains a great challenge to improve the 3D printing technology, which is capable of giving rise to an excellent performance in silicon-based thick electrodes.

In view of the application bottleneck of silicon-based hybrid materials, totally replacing the commercial graphite (Gt) with SiO is still hard to reach.^[31–35] Thus, in this work, we chose cheap commercial Gt and SiO as raw materials. The 3D multilayer Gt@GS (Gt@Gt-SiO) array electrode was fabricated through two nozzles alternately patterning. For the printed 3D multilayer array electrode, SiO particles were distributed in GS arrays, which were further surrounded by Gt arrays. The obtained 3D Gt@GS electrode, as a freestanding architecture, shows the high capacity (19.5 mAh cm^{-2} at 0.9 Acm^{-2}) and good cycling stability (3.52 mAh cm^{-2} at 3.6 mAcm^{-2} after 120 cycles). Besides, the 3D plane-shaped battery was fabricated as an external power supply for the aircraft model,

demonstrating the advantages of combining the structural loading and the 3D printing technology.

Results and Discussion

The “multilayer biscuit” (the inset map in Figure 1a) is common in everyday life and popular with people. As we all know, the multilayer biscuit consists alternately of two types of biscuits and possesses a regular grid in each layer. Inspired by the structure feature of multilayer biscuit, the 3D multilayer biscuit electrode was fabricated to improve the volume expansion of SiO particles and their associated problems. The auto-computer-aided-design (auto-CAD) software was used to design electrode architecture. And then, the as-prepared functional inks were alternately extruded through two nozzles (Figure 1a). The Gt array firstly was patterned on the conductive glass, then the GS array was patterned on the surface of the Gt array. Repeating the above steps, the 3D Gt@GS electrode was successfully prepared, which shows a multilayer biscuit structure (The inset image of Figure 1a). As expected, the 3D Gt@GS electrode has a structure maintenance after repeated cycles, whereas the 3D GS electrode displays a structure damage in Figure 1(b). The primary reason for the speculation is that the mechanical strain of SiO particles in GS array not only obtains the mitigation of graphite particles in the horizontal direction,

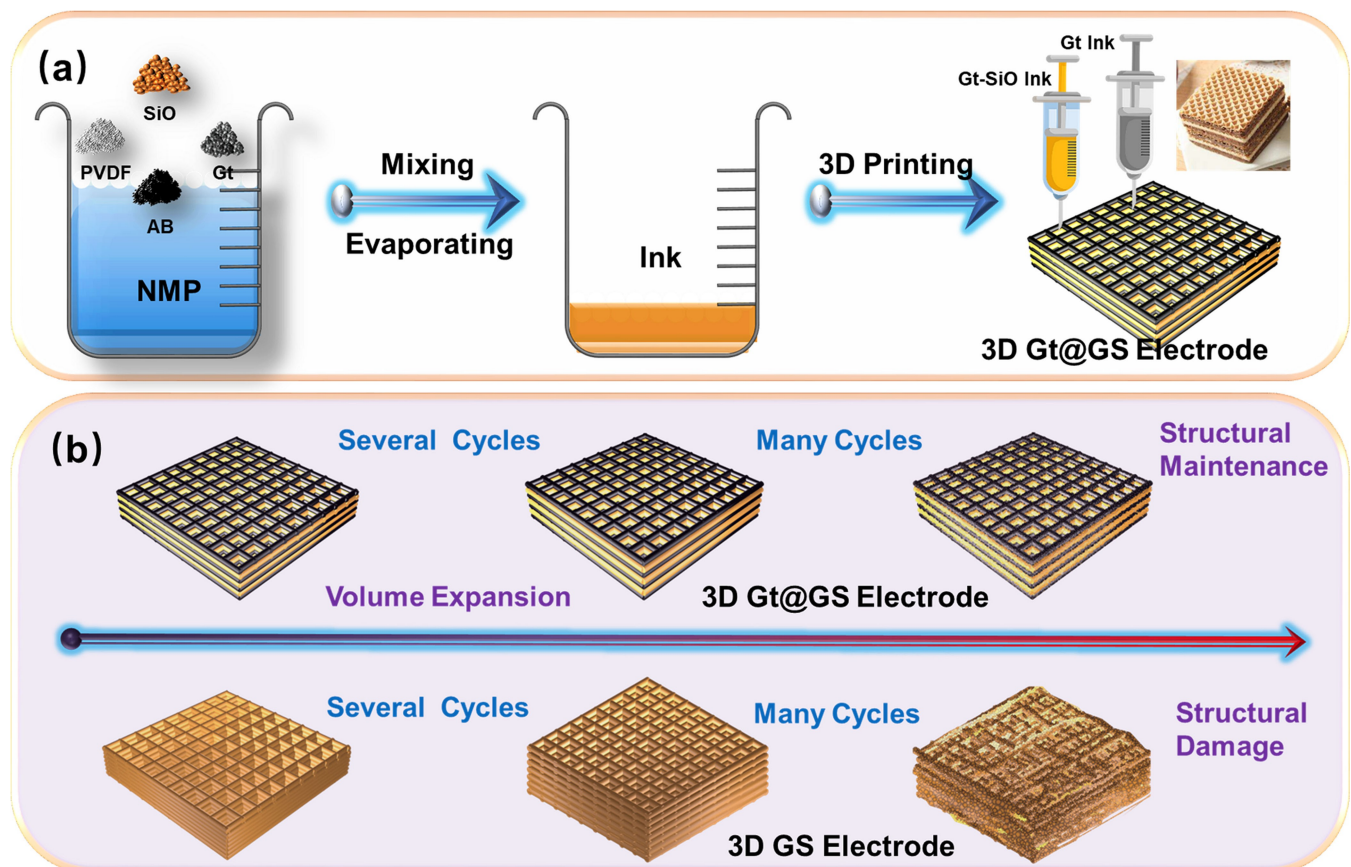


Figure 1. a) The fabrication process of the 3D Gt@GS electrode. b) The structural evolution of the 3D Gt@GS electrode and the 3D GS electrode during cycling.

but also acquires the limitation of the Gt arrays in the vertical direction.^[38–40] Hence, the performance deterioration has a dramatically improvement through introducing the design strategy of the 3D multilayer array electrodes.

Figure 2 shows some manufacturing details and features of the 3D printing technology. The shapes of the printing models were pre-designed by using the auto-CAD software without any mold. Figure 2(a) shows the pre-designed pattern for the square electrode. Figure 2(b) is a digital image of the direct ink writing 3D printer equipment with two nozzles, which was modified by ourselves. The Gt ink was firstly extruded from the left nozzle to print a layer of Gt array on the surface of conductive glass. According to the height of the last printing, the starting point of the right needle was then adjusted manually, so that it was at the finishing point of the left needle. Next, the GS array was patterned on the upper layer of Gt array. Finally, the square array electrode was printed through layer-by-layer assembly. Different thickness electrodes were printed in Figure S1(a), and their thicknesses mainly depend on the number of layers and the needle diameter of the syringe. Figure 2(c) demonstrates the area of the seven-layer electrode

was roughly 0.55 cm^2 after vacuum drying. Due to the complex structure of the heterotypic battery, the preparation process of complex shaped electrode has very strict requirements for the rheology and viscosity of ink.^[39,41,42] When the viscosity is too high or too low, the as-prepared ink is difficult to extrude out, or the extruded lines cannot be preserved. When it is not dense enough, the bubbles inside of the ink will burst under the pressure of squeezed gas, leading to the printed electrodes damage. Hence, the proper viscosity and density of the ink is the keys to the efficient and massive preparation of 3D heterotypic thick electrodes. Figure 2(d–g) displays the 3D printing patterns of “NUAA”, helicopter, cruise aircraft and fighter plane, which correspond to the pre-designed patterns in Figure S1(b–e). Notably, “NUAA” is an abbreviation of Nanjing University of Aeronautics and Astronautics. And different airplane patterns demonstrate the maturity of the 3D printing technology. Therefore, the 3D plane electrode was prepared for the subsequent assembly of the 3D plane-shaped battery (Figure 2h), and the printing model was also designed by using auto-CAD software (Figure S1f). The successful printing of these heterotypic electrodes demonstrates that the 3D

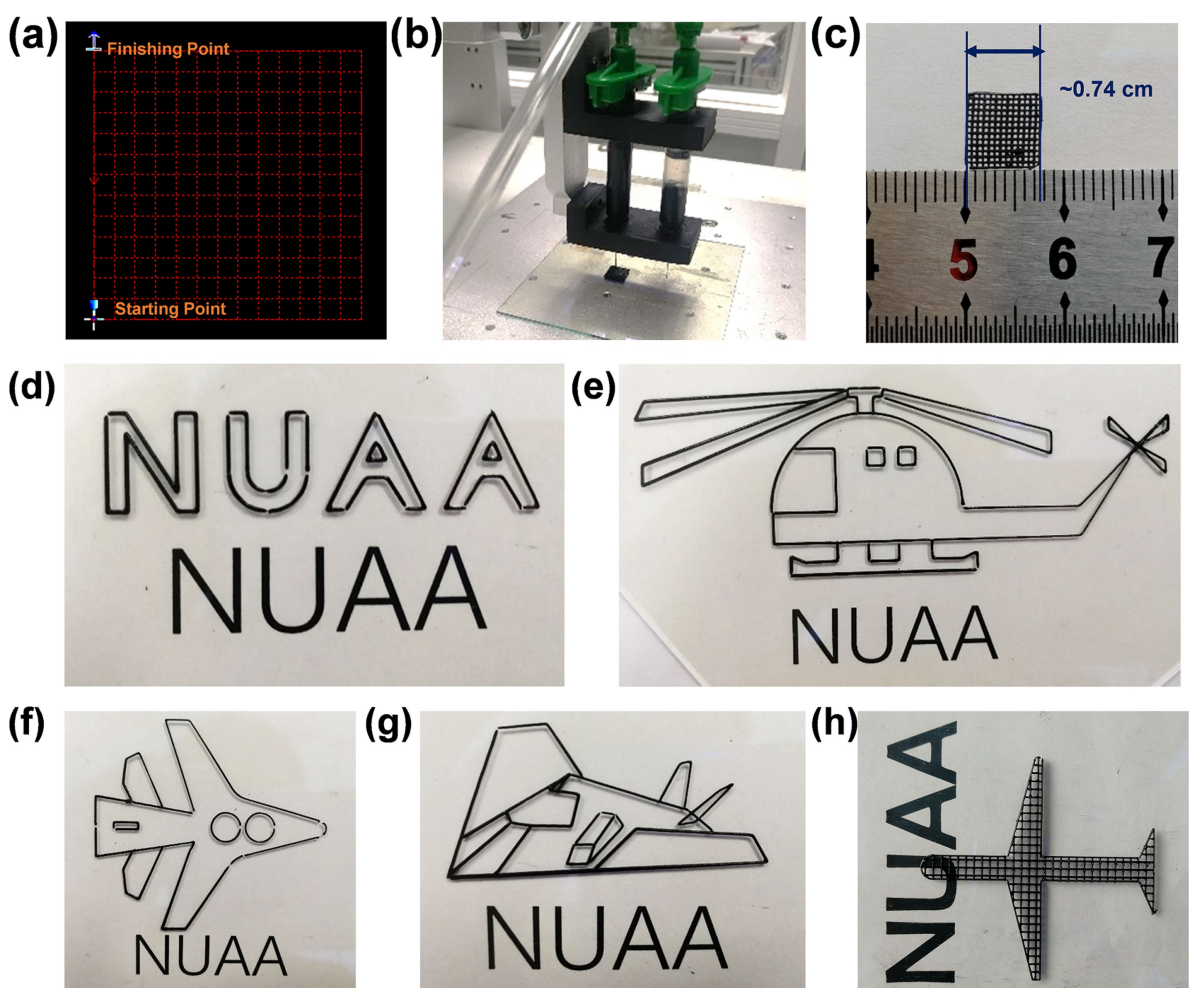


Figure 2. a) The pre-designed pattern for the square array electrode (the red arrow pointing the movement path of the needles). b) The digital image of the 3D printing equipment with two nozzles. c) The size of the printed 3D Gt@GS electrode. D–h) The 3D printing patterns for NUAA, helicopter, cruise aircraft, fighter plane, and 3D Gt@GS plane anode.

printing is a precise, controllable and mass-prepared technology in the field of structural energy storage.

To explore the structure of the 3D "multilayer biscuit" electrode, the scanning electron microscopy (SEM) images are shown in Figure 3. From the top-down view, the 3D Gt@GS electrode has a perfectly integrated grid of the interwoven lines with a diameter of about 120 μm (Figure 3a, b). It can also be observed that the pores in the grid display a regular shape. The magnified SEM images show that active materials (black segment) have a uniform dispersion, which are well encapsulated by binders and conductive agents (gray segment) (Figure 3c, d). Switching to the cross-section shown in Figure 3(e), the thickness of a single printed layer between the different layers is $\sim 80 \mu\text{m}$, showing a perfect welding combination (Figure 3f). Afterward, the 3D multilayer biscuit structure was further confirmed by the energy dispersive spectroscopy. Figure 3(g) presents a uniform distribution of C and Si elements in the 3D GS electrode. Note that, Figure 3(h) shows that the C element has a uniform distribution in 3D Gt@GS electrode, while the Si element is distributed in the form of zebra crossings. These results mean that the ideal 3D multilayer biscuit structure has been successfully constructed. Figure S2(a, b) presents the phase component of the 3D Gt@GS electrode, demonstrating the existence of SiO and graphite and no other

impurity peaks are observed.^[43,44] The refined spectrum of Si 2p suggests that SiO sample is a mixture of Si with different valence states (Figure S2c).^[44] The deconvoluted C 1s spectrum indicates the obvious peak at 284.6 eV (Figure S2d), which is attributed to graphite, and other weak peaks are mainly due to the presence of conductive agents.^[45]

To evaluate the electrochemical performance of the 3D multilayer biscuit structure, the 3D GS and 3D Gt@GS electrodes were assembled into coin cells. In Figure 4(a), the 3D Gt@GS anode with mass loading of approximately 19.1 mg exhibits an initial discharge capacity of 19.5 mAh cm^{-2} at 0.9 A cm^{-2} , delivering an initial Coulombic efficiency (ICE) of 67.4%. In comparison, the 3D GS anode displays an initial discharge capacity of 24.0 mAh cm^{-2} at 0.9 A cm^{-2} (Figure S3a), while a low ICE (64.2%) is acquired. As shown in Figure 4(b), the 3D Gt@GS anode exhibits an enhanced cycling performance compared to the 3D GS electrodes, which presents a reversible capacity of 9.28 mAh cm^{-2} after 50 cycles. Increasing the current density to 1.8 and 3.6 mA cm^{-2} (Figure 4c, d), the capacities of the 3D Gt@GS electrodes are 6.43 and 3.93 mAh cm^{-2} after 50 cycles. And the corresponding capacity retention rates at 1.8 and 3.6 mA cm^{-2} are 69.3% and 42.3%, respectively. Especially in Figure 4(d), the 3D Gt@GS electrode after 120 cycles also achieves a reversible capacity of

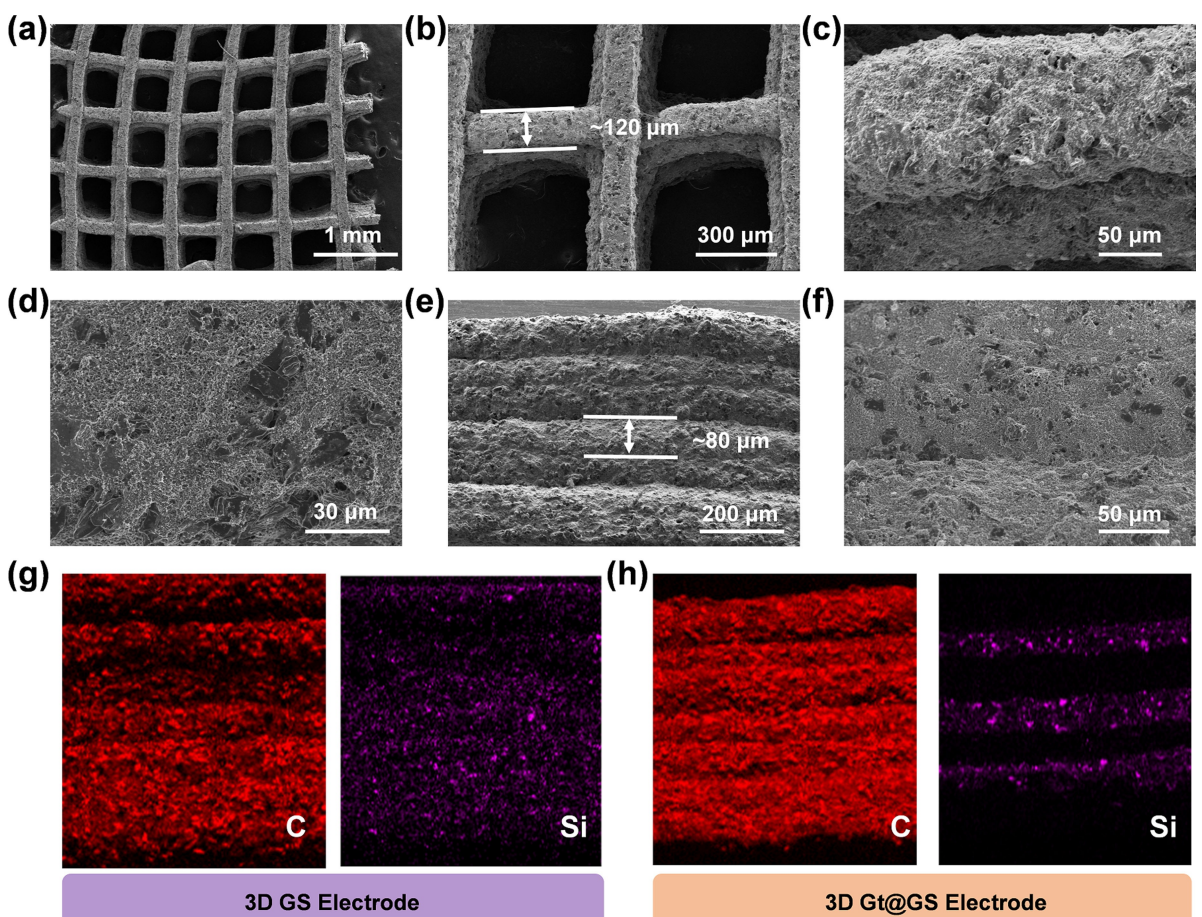


Figure 3. a-d) The top-down SEM images and e-f) the cross-sectional SEM images of the 3D Gt@GS electrode. Elemental mapping images of g) the 3D GS electrode and h) the 3D Gt@GS electrode.

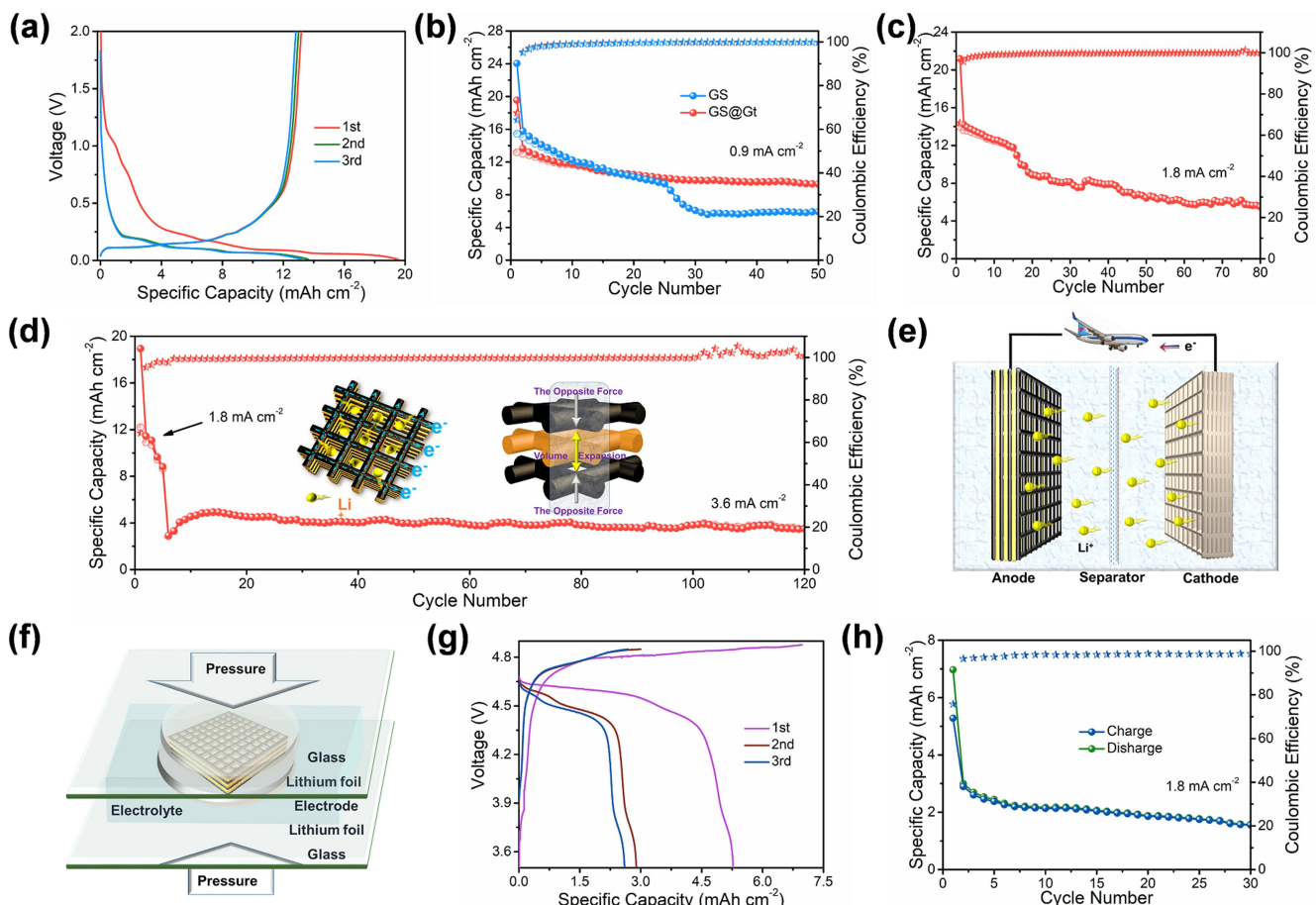


Figure 4. Electrochemical performance of the assembled half-cell and full-cell. a) Charge-discharge profiles of the 3D Gt@GS electrode at 0.9 mA cm^{-2} . b) Cycling performances of the 3D GS electrode and the 3D Gt@GS electrode at 0.9 mA cm^{-2} . c, d) Cycling performances of the 3D Gt@GS electrode at 1.8 and 3.6 mA cm^{-2} . e) The charge storage mechanism of the full-cell (3D Gt@GS//3D LNMO). f) Schematic illustration of pre-lithiation of the 3D Gt@GS electrode. g) Charge-discharge profiles and h) cycling performance of the assembled full-cell at 1.8 mA cm^{-2} .

3.52 mAh cm^{-2} at 3.6 mA cm^{-2} . When the half-cell was disassembled and shown in Figure S3(b), the 3D Gt@GS electrode basically maintains the structural integrity. For this special structure in the insert maps of Figure 4(d), graphite particles dispersed in the 3D skeleton can build a large number of bridges in all directions, facilitating electron transport.^[45] Furthermore, the square pores in the 3D electrode can provide a sufficient space for electrolyte infiltration at the macroscale, and accommodate the volume expansion of SiO particles during cycling. Besides, the Gt arrays on both sides can provide an opposite force, thereby limiting the volume expansion of the GS arrays during lithiation. To further investigate the kinetic behavior of electrodes, the electrochemical impedance spectroscopies (EIS) were presented in Figure S3(c).^[22,43] The shrinkage of the semicircle after 120th cycle corresponds to a decrease in the charge transfer interfacial resistance (R_{ct}), which means that the 3D skeleton provides a rapid ion diffusion channel. Figure S3d shows the cyclic voltammetry (CV) of the 3D Gt@GS electrode. The reduction peaks at 0.76 and 0.14 V during lithiation process are mainly attributed to the formation of lithium carbide (Li_xC) and lithium silicide (Li_xSi) phase.^[43,47,48] The broad oxidation peaks at 0.27 V and 0.56 V are caused by

the delithiation of Li_xC and Li_xSi . Additionally, there is an irreversible reaction located at 1.0 V, corresponding to the formation of solid electrolyte interphase (SEI) film, lithium silicates, and Li_2O . Other curves in the following scans have a slight offset, indicating a good cycling reversibility.

To investigate the stability of the 3D multilayer biscuit structure, the optical microscope was performed to focus on the structure evolution of the electrode before and after first discharge. As shown in Figure S4(a, c), the 3D GS anode has a large thickness change from 724.8 to 957.4 μm . The grid displays several huge cracks and a distinct distortion in Figure S4(d). In contrast, the thickness change of the 3D Gt@GS electrode is $\sim 155 \mu\text{m}$ (Figure S5a, c). It can be found that the 3D Gt@GS electrodes in Figure S5(a, c) have a smaller swelling (18.8%) than that of the 3D GS electrode ($\sim 32.1\%$). In addition, the 3D Gt@GS electrode (Figure S5d) exhibits a slight deformation and basically maintains the grid structure. Thus, it is reasonable to assume that the high reversible capacity and good cycling ability of the 3D Gt@GS electrode could be ascribed to 3D multilayer biscuit structure.

Intrigued by the unique structure, the full-cell performance was further investigated by using the 3D Gt@GS electrode. The

charge storage mechanism of the full-cell is illustrated in Figure 4(e), which has been established based on as-prepared 3D Gt@GS anode and 3D-printed lithium nickel manganese oxide ($\text{LiNi}_{0.5}\text{Mn}_{1.5}\text{O}_4$, LNMO) cathode. Notably, the LNMO material was used as a cathode due to its high voltage platform (4.7 V) and cobalt-free.^[49,50] Before matching the full battery, the half-cell performance of the 3D LNMO cathode was firstly tested. Figure S6(a) shows the LNMO cathode (43.4 mg) delivers discharge capacities of 3.2, 4.6 and 4.7 mAh cm^{-2} in the first three cycles at 1.8 mA cm^{-2} . After 70 cycles, the reversible capacity remains 4.8 mAh cm^{-2} (Figure S6b). To simplify the matching process, the 3D Gt@GS firstly had a simple internal short pre-lithiation to eliminate its initial irreversible loss (Figure 4f).^[43,51] To balance the safe operation and electrochemical performance of the battery as much as possible, the voltage range was set as 3.5–4.85 V. The assembled full-cell (3D Gt@GS//3D LNMO) delivers a high initial charge/discharge capacities of 7.0 and 5.3 mAh cm^{-2} (Figure 4g), corresponding to an ICE of 75.7%. With assumed the average working voltage at 4.6 V, the full cell has a volumetric energy density of 322.5 Wh L^{-1} based on the cathode. Figure 4(h) exhibits the cycling stability of the full-cell at a current density of 1.8 mA cm^{-2} . After 30 cycles, it delivers a reversible capacity of 1.56 mAh cm^{-2} . To explore the reasons of the rapid deterioration of capacity, the full-cell (3D Gt@GS//3D LNMO) was also

dis-assembled. Figure S6(c) exhibits that the structures of the cathode and the anode remain basically unchanged after 30 cycles, while the amount of the electrolyte becomes significantly less.

To further demonstrate the practical application of 3D printing technology, we have combined structural elements and energy storage to fabricate 3D plane batteries. Firstly, the 3D LNMO plane cathode (Figure 5a) was fabricated by using a direct ink writing technology. Figure S7(a) shows the plane-shape pattern of the battery case, which was pre-designed by using SOLIDWORKS software. After slicing, the 3D plane-shaped battery case was printed by a fused deposition modeling 3D printer (Figure S7b) and shown in Figure 5(b). The battery case was made of a shell with a groove and a lid that can be placed inside the groove. Then, the heterotypic battery was successfully assembled, according to Figure 5(c). Finally, the battery was sealed with vacuum silicone. And we drew two electric wires from the cathode and anode (Figure 5d). Before assembling into the aircraft model, the 3D plane-shape battery can serve as a power supply for LED lights (Figure 5e, Supporting Information movie_01) and a small industrial fan (Figure S7c, Supporting Information movie_02). Especially, fourteen LED lights can be still successfully lightened at a weight of about 5 kg (Figure 5f), demonstrating the fabricated heterotypic battery is robust. For better interpreting the significance of

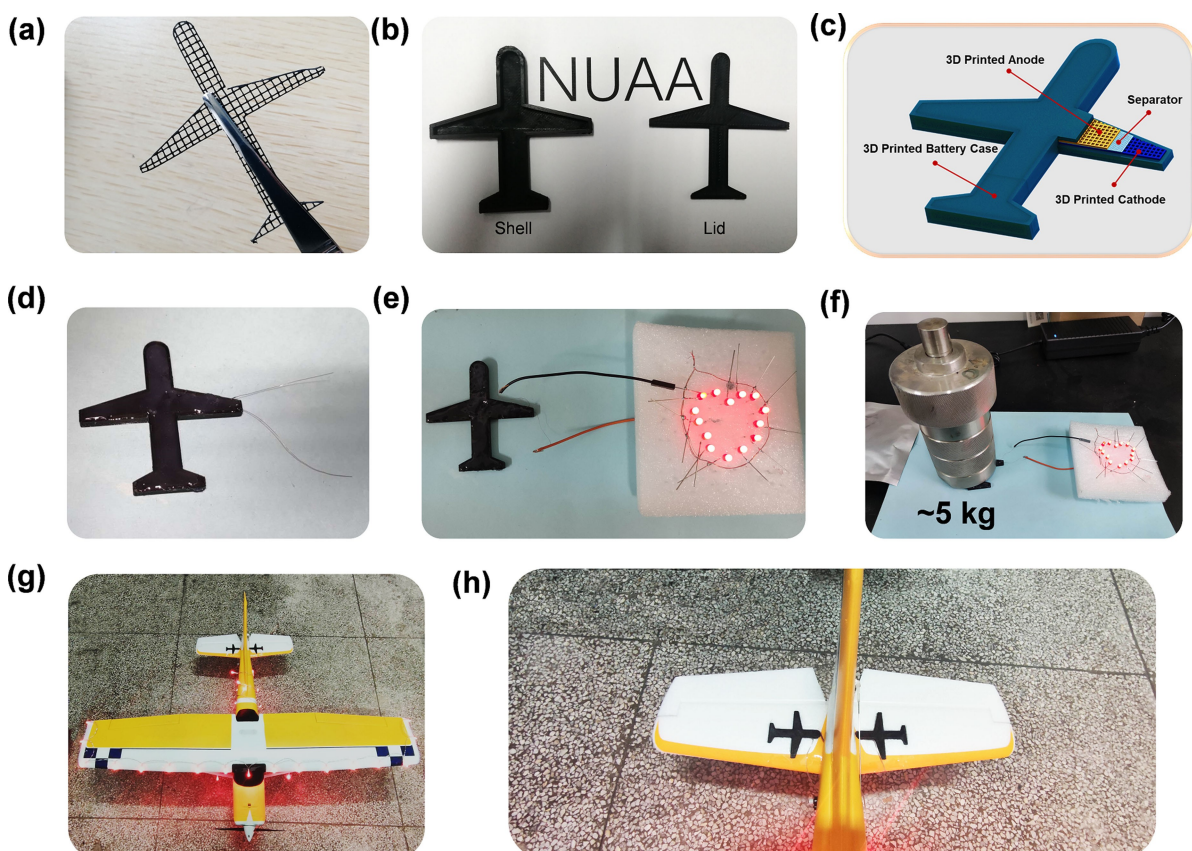


Figure 5. a) The 3D LNMO cathode. b) The 3D printed battery case by using a fused deposition 3D printer. c) The inner structure diagram of 3D plane battery. d) The photo of the assembled 3D plane battery. e, f) The 3D plane battery with LED lights at a weight of about 5 kg. g, h) Two 3D plane-shape batteries assembled on aircraft models, providing electrical power for the aircraft lighting system.

structural energy storage, two parts were removed from the rear wings of the aircraft model, which were replaced with two 3D plane-shape batteries (Figure 5g). The two 3D-plane-shaped batteries not only can be used as a part of the aircraft, but also provide the electrical power for the aircraft lighting system (Figure 5h). Therefore, it is necessary to combine the structural loading and energy storage as a solution to meet the commercial viability.

Conclusion

In summary, we have taken advantage of the multilayer biscuit structure feature to the 3D Gt@GS electrode with high loading. Such a unique structure can improve the transmission dynamics in all directions and limit the volume expansion of SiO particles. Hence, the 3D printed multilayer array electrode exhibits an enhanced cycling performance, due to its 3D strong and tough skeleton. Furthermore, it is startling that the assembled full cell (3D Gt@GS//LNMO) delivers a high reversible capacity of 5.3 mAh cm^{-2} at 1.8 mA cm^{-2} . Besides, we have fabricated the 3D plane-shape battery, which acts as an ornament of the aircraft model and supplying power. These results demonstrate that the structural battery combined structural loading and 3D printing technology provides a timely solution to meet the commercial demand for high energy densities in energy storage.

Experimental Section

Preparation of the 3D-printable inks

The Gt (chemically pure) was purchased from National medicine reagent. SiO particles were obtained by mechanically chemically breaking bulk SiO (Aladdin, 325 mesh). Firstly, the Gt and SiO particles with a mass ratio of 4:1 were uniformly mixed into a mixture. Then, the active material, acetylene black (AB), and polyvinylidene fluoride (PVDF) with a mass ratio of 7:2:1 were dispersed in N-Methyl pyrrolidone (NMP) to form a slurry, followed by stirring at room temperature overnight. Afterwards, the slurry was further heated to evaporate the solvent to obtain the 3D-printed GS ink with a suitable viscosity. This step was repeated to prepare the 3D-printed Gt ink without SiO particles.

Preparation of 3D-printed electrodes

The 3D-printed GS ink, stored in a syringe, was centrifuged at 1500 rpm to remove air. The 3D GS electrode architecture was designed using auto-CAD software, following by machining through a 3D printer. The highly concentrated GS ink was extruded through a nozzle with a diameter of $\sim 100 \mu\text{m}$ and an optimal printing speed (1 mm s^{-1}) as well as an extrusion pressure (8 bar). The 3D GS electrode on the conductive glass had a pre-drying at room temperature, and subsequently further removed solvent in a vacuum drying oven at 120°C for 12 h.

Before preparing the 3D Gt@GS electrodes, the calibration was performed to minimize the effect of the inconsistency on the performance. The calibration is mainly divided into the following steps: We will put the two needles in parallel, which were vertical

to the workbench. The starting point of left needle was determined, so the coordinate value (x, y, z) was recorded, and the ink was squeezed out. Then, the starting point of right needle was determined according to the distance of the two needles and the diameter of the needle. When the two layers coincided completely after extruding a layer of ink from the right needle, its coordinate value (x, y, z) was also recorded. During subsequent printing process, the height (z) was increased when fixing x and y . If we continued to print the same electrode, just moved the working platform. Location changes in the work platform did not cause changes in the needle position, so the recalibration was not required.

The preparation steps of 3D Gt@GS electrode are similar to the 3D GS electrode. The differences were that the 3D Gt@GS electrode was printed alternately through two nozzles. The one of them contains Gt and the other contains GS. The Gt layer was firstly extruded on the conductive glass substrates, and then GS layer was extruded on the Gt layer by regulating the position of the needle. The content of SiO in the electrode can be calculated according to the following formula: $C = \frac{L_{GS}}{L_F} \times 14\%$, where C is the content of SiO in the electrode, L_{GS} is the number of GS layers and L_F is the number of GS and Gt layers.

Supporting Information

Supporting Information is available from the Wiley Online Library or from the author.

Acknowledgements

This work is financially sponsored by the National Natural Science Foundation of China (21875107, U1802256, 51672128, 52072173 and 21773118), Jiangsu Specially-Appointed Professors Program, Jiangsu Province Outstanding Youth Fund (SBK2020010215), Leading Edge Technology of Jiangsu Province (BK20202008), Key Research and Development Program in Jiangsu Province (BE2018122), Natural Science Foundation of Jiangsu Province (BK20170778), Fundamental Research Funds for the Central Universities (NE2016005) and the Priority Academic Program Development of Jiangsu Higher Education Institutions (PAPD). W. H. acknowledges support from Postgraduate Research & Practice Innovation Program of Jiangsu Province (KYCX20_0192).

Conflict of Interest

The authors declare no conflict of interest.

Keywords: 3D printing • high energy density • multilayer biscuit • silicon monoxide • structural energy storage

- [1] J. W. Choi, D. Aurbach, *Nat. Rev. Mater.* **2016**, *1*, 16013.
- [2] F. Duffner, N. Kronemeyer, J. Tübke, J. Leker, M. Winter, R. Schmuck, *Nat. Energy* **2021**, *6*, 123.
- [3] M. Li, J. Lu, Z. Chen, K. Amine, *Adv. Mater.* **2018**, *30*, e1800561
- [4] J. Liu, Z. Bao, Y. Cui, E. J. Dufek, J. B. Goodenough, P. Khalifah, Q. Li, B. Y. Liaw, P. Liu, A. Manthiram, Y. S. Meng, V. R. Subramanian, M. F. Toney,

- V. V. Viswanathan, M. S. Whittingham, J. Xiao, W. Xu, J. Yang, X. Yang, J. Zhang, *Nat. Energy* **2019**, *4*, 180.
- [5] Y. Tian, G. Zeng, A. Rutt, T. Shi, H. Kim, J. Wang, J. Koettgen, Y. Sun, B. Ouyang, T. Chen, Z. Lun, Z. Rong, K. Persson, G. Ceder, *Chem. Rev.* **2020**, *121*, 1623.
- [6] Y. Lu, X. Rong, Y. Hu, L. Chen, H. Li, *Energy Storage Mater.* **2019**, *23*, 144.
- [7] F. Chen, J. Han, D. Kong, Y. Yuan, J. Xiao, S. Wu, D. Tang, Y. Deng, W. Lv, J. Lu, F. Kang, Q. Yang, *Natl. Sci. Rev.* **2021**, *8*, b12.
- [8] C. Meng, N. Muralidharan, E. Teblum, K. E. Moyer, G. D. Nessim, C. L. Pint, *Nano Lett.* **2018**, *18*, 7761.
- [9] E. Pomerantseva, F. Bonaccorso, X. Feng, Y. Cui, Y. Gogotsi, *Science* **2019**, *366*, n8285.
- [10] K. Moyer, C. Meng, B. Marshall, O. Assal, J. Eaves, D. Perez, R. Karkkainen, L. Roberson, C. L. Pint, *Energy Storage Mater.* **2020**, *24*, 676.
- [11] C. González, J. J. Vilatela, J. M. Molina-Aldareguía, C. S. Lopes, J. LLorca, *Prog. Mater. Sci.* **2017**, *89*, 194.
- [12] Z. Liu, Q. Yu, Y. Zhao, R. He, M. Xu, S. Feng, S. Li, L. Zhou, L. Mai, *Chem. Soc. Rev.* **2019**, *48*, 285.
- [13] Y. Jin, B. Zhu, Z. Lu, N. Liu, J. Zhu, *Adv. Energy Mater.* **2017**, *7*, 1700715.
- [14] M. T. McDowell, S. W. Lee, W. D. Nix, Y. Cui, *Adv. Mater.* **2013**, *25*, 4966.
- [15] X. Zhang, D. Kong, X. Li, L. Zhi, *Adv. Funct. Mater.* **2019**, *29*, 1806061.
- [16] P. Li, G. Zhao, X. Zheng, X. Xu, C. Yao, W. Sun, S. X. Dou, *Energy Storage Mater.* **2018**, *15*, 422.
- [17] J. Wu, Y. Cao, H. Zhao, J. Mao, Z. Guo, *Carbon Energy* **2019**, *1*, 57.
- [18] X. Zhang, Z. Ju, Y. Zhu, K. J. Takeuchi, E. S. Takeuchi, A. C. Marschilok, G. Yu, *Adv. Energy Mater.* **2021**, *11*, 2000808.
- [19] Y. Kuang, C. Chen, D. Kirsch, L. Hu, *Adv. Energy Mater.* **2019**, *9*, 1901457.
- [20] C. Zhang, S. Park, A. Seral Ascaso, S. Barwick, N. McEvoy, C. S. Boland, J. N. Coleman, Y. Gogotsi, V. Nicolosi, *Nat. Commun.* **2019**, *10*, 849.
- [21] C. Huang, A. Kim, D. J. Chung, E. Park, N. P. Young, K. Jurkschat, H. Kim, P. S. Grant, *ACS Appl. Mater. Interfaces* **2018**, *10*, 15624.
- [22] S. S. Zhang, *InfoMat* **2020**, *2*, 942.
- [23] J. Park, C. Jeon, W. Kim, S. Bong, S. Jeong, H. Kim, *J. Power Sources* **2021**, *482*, 228948.
- [24] S. H. Park, R. Tian, J. Coelho, V. Nicolosi, J. N. Coleman, *Adv. Energy Mater.* **2019**, *9*, 1901359.
- [25] H. Li, L. Peng, D. Wu, J. Wu, Y. Zhu, X. Hu, *Adv. Energy Mater.* **2019**, *9*, 1802930.
- [26] Y. Zhang, F. Li, K. Yang, X. Liu, Y. Chen, Z. Lao, K. Mai, Z. Zhang, *Adv. Funct. Mater.* **2021**, 2100434.
- [27] B. Shi, Y. Shang, Y. Pei, S. Pei, L. Wang, D. Heider, Y. Y. Zhao, C. Zheng, B. Yang, S. Yarlagadda, T. Chou, K. K. Fu, *Nano Lett.* **2020**, *20*, 5504.
- [28] T. Wu, Z. Zhao, J. Zhang, C. Zhang, Y. Guo, Y. Cao, S. Pan, Y. Liu, P. Liu, Y. Ge, W. Liu, L. Dong, H. Lu, *Energy Storage Mater.* **2021**, *36*, 265.
- [29] L. J. Deiner, T. Jenkins, A. Powell, T. Howell, M. Rottmayer, *Adv. Eng. Mater.* **2019**, *21*, 1801281.
- [30] Y. Yu, H. Zhang, X. Yang, J. Gou, X. Tong, X. Li, H. Zhang, *Energy Storage Mater.* **2019**, *19*, 88.
- [31] Y. C. Y. C. Yaokun Pang, *Adv. Mater.* **2020**, *30*, 1906244.
- [32] M. P. Browne, E. Redondo, M. Pumera, *Chem. Rev.* **2020**, *120*, 2783.
- [33] V. Egorov, U. Gulzar, Y. Zhang, S. Breen, C. O'Dwyer, *Adv. Mater.* **2020**, 2000556.
- [34] L. Mao, Q. Meng, A. Ahmad, Z. Wei, *Adv. Energy Mater.* **2017**, *7*, 1700535.
- [35] Z. Lyu, G. J. H. Lim, J. J. Koh, Y. Li, Y. Ma, J. Ding, J. Wang, Z. Hu, J. Wang, W. Chen, Y. Chen, *Joule* **2020**, *1*, 1.
- [36] P. Li, J. Hwang, Y. Sun, *ACS Nano* **2019**, *13*, 2624.
- [37] N. Kim, S. Chae, J. Ma, M. Ko, J. Cho, *Nat. Commun.* **2017**, *8*, 812.
- [38] J. L. Goldman, B. R. Long, A. A. Gewirth, R. G. Nuzzo, *Adv. Funct. Mater.* **2011**, *21*, 2412.
- [39] C. Chen, J. Jiang, W. He, W. Lei, Q. Hao, X. Zhang, *Adv. Funct. Mater.* **2020**, 1909469.
- [40] X. Gao, Q. Sun, X. Yang, J. Liang, A. Koo, W. Li, J. Liang, J. Wang, R. Li, F. B. Holness, A. D. Price, S. Yang, T. Sham, X. Sun, *Nano Energy* **2019**, *56*, 595.
- [41] J. Orangi, F. Hamade, V. A. Davis, M. Beidaghi, *ACS Nano* **2020**, *14*, 640.
- [42] B. Yao, S. Chandrasekaran, J. Zhang, W. Xiao, F. Qian, C. Zhu, E. B. Duoss, C. M. Spadaccini, M. A. Worsley, Y. Li, *Joule* **2019**, *3*, 459.
- [43] W. He, T. Zhang, J. Jiang, C. Chen, Y. Zhang, N. Liu, H. Dou, X. Zhang, *ACS Appl. Mater. Interfaces* **2020**, *3*, 4394.
- [44] Z. Liu, D. Guan, Q. Yu, L. Xu, Z. Zhuang, T. Zhu, D. Zhao, L. Zhou, L. Mai, *Energy Storage Mater.* **2018**, *13*, 112.
- [45] S. Karuppiah, C. Keller, P. Kumar, P. Jouneau, D. Aldakov, J. Ducros, G. Lapertot, P. Chenevier, C. Haon, *ACS Nano* **2020**, *14*, 12006.
- [46] C. Sun, S. Liu, X. Shi, C. Lai, J. Liang, Y. Chen, *Chem. Eng. J.* **2020**, *381*, 122641.
- [47] K. Kitada, O. Pecher, P. C. M. M. Magusin, M. F. Groh, R. S. Weatherup, C. P. Grey, *J. Am. Chem. Soc.* **2019**, *141*, 7014.
- [48] T. Ma, H. Xu, X. Yu, H. Li, W. Zhang, X. Cheng, W. Zhu, X. Qiu, *ACS Nano* **2019**, *13*, 2274.
- [49] G. Liang, Z. Wu, C. Didier, W. Zhang, J. Cuan, B. Li, K. Y. Ko, P. Y. Hung, C. Z. Lu, Y. Chen, G. Leniec, S. M. Kaczmarek, B. Johannessen, L. Thomsen, V. K. Peterson, W. K. Pang, Z. Guo, *Angew. Chem. Int. Ed.* **2020**, *59*, 10594.
- [50] J. Wang, P. Nie, G. Xu, J. Jiang, Y. Wu, R. Fu, H. Dou, X. Zhang, *Adv. Funct. Mater.* **2018**, *28*, 1704808.
- [51] P. Nie, X. Liu, R. Fu, Y. Wu, J. Jiang, H. Dou, X. Zhang, *ACS Energy Lett.* **2017**, *2*, 1279.

Manuscript received: September 15, 2021

Revised manuscript received: November 28, 2021

Accepted manuscript online: December 4, 2021

Version of record online: January 5, 2022